PHYSICAL REVIEW B **102**, 064402 (2020)

Magnetic anisotropy of a Dy atom on a graphene/Cu(111) surface

A. B. Shick,[1] J. Kolorenč,[1] A. Yu. Denisov,[2] and D. S. Shapiro[3]
[1]Institute of Physics, Czech Academy of Sciences, Na Slovance 2, 182 21 Prague, Czech Republic
[2]Quantum Magnetometry Laboratory, Ural Federal University, 19 Mira St., 620002 Yekaterinburg, Russian Federation
[3]Institute of Radio Engineering and Electronics, Russian Academy of Sciences, 11-7 Mokhovaya St., 125009 Moskow, Russian Federation

(Received 29 April 2020; accepted 16 July 2020; published 4 August 2020)

The electronic structure and magnetism of individual Dy atoms adsorbed on the graphene/Cu(111) surface is investigated using the combination of the density functional theory with the Hubbard-I approximation to the Anderson impurity model (DFT + U + HIA). We find that the results of the DFT + U + HIA depend on the choice of the double-counting term. For fully localized limit, the divalent Dy^{2+} adatom is found, with the total magnetic moment of 9.71 μ_B. The spin and orbital magnetic moments are evaluated, and compared with the x-ray magnetic circular dichroism data. The calculated positive magnetic anisotropy energy determines the out-of-plane orientation of the Dy adatom magnetic moment, in agreement with available experimental data.

DOI: 10.1103/PhysRevB.102.064402

I. INTRODUCTION

Surface supported single atom magnets (SAM) play a promising role in reducing the magnetic domain size for the ultrahigh density magnetic memory components. Magnetic rare-earth (RE) atoms adsorbed on metallic [1,2] and insulating [3] solid surfaces recently attracted a lot of attention in an attempt to create the atomic-size magnets. Another important aspect is the use of SAM as qubits for quantum information processing [4]. This proof-of-principle experimental realization of Grover's search algorithm [5] on a single RE adatoms may open new opportunities in further practical realization of quantum qubits.

The magnetic remanence, together with long magnetic relaxation time are prerequisites for the magnetic stability of adatoms. Experimental studies [6] have shown that Dy adatoms deposited on the graphene on the top of Ir substrate display a SAM behavior. This experimental observation provides an opportunity to manipulate individual Dy moments by using microwave electromagnetic field and dc-electric current. The large magnetic anisotropy energy (MAE) is the key quantity to achieve the magnetic stability. Another condition is the doubly degenerate ground state, which has to be protected by the crystal field of the substrate against the quantum tunneling, and decoupled from conduction electrons and phonons of the substrate in order to reduce the spin-flip scattering.

The MAE of single magnetic RE impurities adsorbed on surfaces can be measured mainly by the x-ray magnetic circular dichroism (XMCD). The interpretation of XMCD data relies on the atomic sum rules [7]. The atomic multiplet calculations with several fitting parameters are employed to determine the crystal electric field (CF), and the spin-orbit coupling (SOC) strength. The outcome of these multiplet calculations are the spin and orbital magnetic moments, together with the ground and exited states energy spectrum [8].

In this work, we present the theoretical approach based on the combination of the density functional theory (DFT) with the multiorbital impurity Hamiltonian, which includes the electron-electron interaction effects together with the CF and SOC. Previously, the method was used to treat the magnetic properties of Dy adatom deposited on the graphene on the top of Ir(111) substrate [Dy@GR/Ir(111)], and now we apply it to examine the anisotropic magnetic character of Dy on the graphene on Cu(111) [Dy@GR/Cu(111)].

We aim to examine the role of the double-counting in density functional theory with the Hubbard-I approximation to the Anderson impurity model (DFT + U + HIA) on the Dy-f-shell valence, spin and orbital magnetic moments, and the MAE. We find that the results of charge-self-consistent DFT + U + HIA strongly depend on the choice of the double-counting: the so-called around-mean-field (AMF) [9] yields the trivalent Dy^{3+}, while the divalent Dy^{2+} is found with the fully-localized-limit (FLL) [10] double-counting. We calculate the uniaxial MAE making use of the crystal-field theory model, and show that it is in semiquantitative agreement with the zero-field-splitting (ZFS) obtained from the solution of the Anderson impurity model. This MAE is calculated negative for the AMF, and positive for the FLL calculations. In the latter case, the out-of-plane direction of the magnetic moment and XMCD spectrum are in agreement with experimental data. We use this agreement to select FLL as the appropriate choice for the double counting.

II. DFT + U + HIA METHOD

We extend the DFT + U method making use of a combination of DFT with the exact diagonalization of the Anderson impurity model. We assume that electron interactions in the s, p, and d shells are well approximated in DFT. We used the rotationally invariant implementation of the DFT + U method in the full-potential linearized augmented plane wave basis that includes both scalar-relativistic and spin-orbit coupling effects [11,12].

The effects of the Coulomb interactions on the electronic structure are described with the aid of a ionic model describing the complete seven-orbital 4f shell. This multiorbital model includes the full spherically symmetric Coulomb interaction, the spin-orbit coupling, and the crystal field. The corresponding Hamiltonian can be written as [13],

$$\begin{aligned}\hat{H}_{\rm imp} = &\sum_{m\sigma} \epsilon_f f^\dagger_{m\sigma} f_{m\sigma}\\ &+ \sum_{mm'\sigma\sigma'} \left[\xi \mathbf{l}\cdot\mathbf{s} + \hat{\Delta}_{\rm CF} + \frac{\Delta_{\rm EX}}{2}\hat{\sigma}_z\right]^{\sigma\;\sigma'}_{mm'} f^\dagger_{m\sigma} f_{m'\sigma'}\\ &+ \frac{1}{2}\sum_{\substack{mm'm''\\ m'''\sigma\sigma'}} U_{mm'm''m'''} f^\dagger_{m\sigma} f^\dagger_{m'\sigma'} f_{m'''\sigma'} f_{m''\sigma}, \qquad (1)\end{aligned}$$

where $f^\dagger_{m\sigma}$ creates an electron in the $4f$ shell. The parameter ξ specifies the strength of the SOC, $\Delta_{\rm CF}$ is the crystal-field potential at the impurity, and $\Delta_{\rm EX}$ is the strength of the exchange field. The energy position ϵ_f ($= -\mu$, the chemical potential) defines the number of f electrons. The last term describes the Coulomb interaction in the f shell. The actual choice of these parameters will be discussed later. This model corresponds to the HIA, and assumes the weakness of the hybridization between the localized f electrons and the itinerant s, p, and d states, so that the quantum impurity model is reduced to the atomic limit.

The Lanczos method [14] is employed to find the lowest-lying eigenstates of the many-body Hamiltonian $H_{\rm imp}$ and to calculate the self-energy matrix $[\Sigma(z)]_{\gamma,\gamma'}$ in the subspace of the f spin orbitals $\{\phi_\gamma = \phi_{m\sigma}\}$ at low temperature ($k_{\rm B}T = \beta^{-1} = 2$ meV). Once the self-energy is found, the local Green's function $G(z)$ for the electrons in the $4f$ manifold reads

$$G(z) = ([G(z)_{\rm DFT}]^{-1} + \Delta\epsilon - \Sigma(z))^{-1}, \qquad (2)$$

where $G_{\rm DFT}(z)$ is the "noninteracting" DFT Green's function, and $\Delta\epsilon$ is chosen so as to ensure that $n_f = -\pi^{-1}{\rm Im\ Tr} \int_{-\infty}^{E_{\rm F}} {\rm d}z[G(z)]$ is equal to the number of 4f electrons derived from Eq. (4). Then, with the aid of the local Green's function $G(z)$, we evaluate the occupation matrix $n_{\gamma_1\gamma_2} = -\pi^{-1}\,{\rm Im} \int_{-\infty}^{E_{\rm F}} {\rm d}z\,[G(z)]_{\gamma_1\gamma_2}$.

The matrix $n_{\gamma_1\gamma_2}$ is used to construct an effective DFT + U potential V_U, which is inserted into Kohn–Sham-like equations [11,12]:

$$[-\nabla^2 + V_{\rm DFT}(\mathbf{r}) + (V_U - V_{dc}) + \xi(\mathbf{l}\cdot\mathbf{s})]\Phi_{\mathbf{k}}(\mathbf{r}) = \epsilon_{\mathbf{k}}\Phi_{\mathbf{k}}(\mathbf{r}). \qquad (3)$$

For the spherically symmetric DFT + U double-counting term we have adopted either the so-called AMF $V_{dc} = (U/2\; n_f + \frac{2l}{2(2l+1)}\;(U - J)\; n_f)$ [9] form, or the FLL $V_{dc} = (U - J)/2\; (n_f - 1)$ [10]. We also note that the DFT potential $V_{\rm DFT}$ in Eq. (4) acting on the f states is corrected to exclude the nonspherical double-counting with V_U [15].

The DFT + U + HIA calculations are performed in the charge self-consistent implementation. Equation (4) is iteratively solved until self-consistency over the charge density is reached. The new DFT Green's function $G_{\rm DFT}$ and the new value of the $5f$-shell occupation are obtained from the solutions of Eq. (4). The next iteration is started by solving Eq. (1) with the updated values of ϵ_f, ξ, $\Delta_{\rm CF}$, and $\Delta_{\rm EX}$.

The new value of $\epsilon_f = -\mu$ in Eq. (1) is determined by the condition $\mu = V_{dc}$. This is an essential condition, and can be justified as follows. The double-counting term V_{dc} accounts approximately for the electron-electron interaction energy $E^{ee}_{\rm DFT}$ already included in the DFT. Thus it can be written as a derivative of this mean energy contribution with respect to the f-shell occupation n_f, $V_{dc} = \partial E^{ee}_{\rm DFT}/\partial n_f$. Indeed, it represents a value of the chemical potential μ that controls the number of f electrons.

The CF matrix $\hat{\Delta}_{\rm CF}$ in Eq. (1) is obtained by projecting the self-consistent solutions of Eq. (4) into the $\{\phi_\gamma\}$ local f-shell basis,

$$[H]_{\gamma_1\gamma_2} = \int_{\epsilon_b}^{\epsilon_t} {\rm d}\epsilon\; \epsilon[N(\epsilon)]_{\gamma_1\gamma_2}, \qquad (4)$$

where

$$[N(\epsilon)]_{\gamma_1\gamma_2} \;=\; -\pi^{-1}{\rm Im}[G(z)_{\rm DFT+U}]_{\gamma_1\gamma_2}$$

is the f-projected density of states (fDOS) matrix, ϵ_b is the bottom of the valence band, and ϵ_t is the upper cutof,f which is naturally defined by the condition $\int_{\epsilon_b}^{\epsilon_t} {\rm d}\epsilon\; {\rm Tr}[N(\epsilon)] = 14$. The exchange splitting $\Delta_{\rm EX}$ corresponds to the interorbital exchange energy between the $4f$ and mainly $5d$ states of Dy, $J_{fd}m_{5d}$ [16], where J_{fd} is ~ 0.1 eV/μ_B [17], and m_{5d} is the magnetic moment of the $5d$ states.

The new occupation matrix is calculated with the aid of Eq. (2), and Eq. (3) is solved for the updated $V_{\rm DFT}$ and V_U. The loop procedure is repeated until the convergence of the $4f$-manifold occupation n_f was better than 0.01. After the self-consistent solution of DFT + U + HIA is obtained, the mean-field total energy $E_{tot} = E_{\rm DFT} + \Delta E^{ee}$ is calculated as a sum of DFT total energy $E_{\rm DFT}$, and the energy correction $\Delta E^{ee} = E^{ee} - E_{dc}$ (the difference between the electron-electron interaction energy E^{ee} and double-counting energy E_{dc} already included in $E_{\rm DFT}$).

III. RESULTS

A. DFT + U + HIA electronic structure

In order to discern the spin and orbital character of the rare-earth Dy adatom on GR/Cu(111) we make use of the $3 \times 3 \times 1$ supercell model with 27 Cu atoms (three layers) for the substrate, and the layer of graphene with 18 C atoms on the top of the Cu(111) surface. The graphene overlayer is placed in the so-called "HCP" (or "1-3") position, where one of the C atoms sits on the top of Cu surface, and another is over second Cu sub-surface layer. The experimental Cu lattice constant of 4.839 a.u., and 6.163 a.u. of separation between the carbon atoms of the graphene sheet and the topmost Cu layer [18] are used. The rare-earth Dy atom is placed in the hollow position atop the graphene/Cu(111) surface. The top view of the supercell is shown in the inset in the Fig. 1.

In the FP-LAPW calculations, 108 special k points in the two-dimensional Brillouin zone were used, with Gaussian smearing for k-points weighting. The "muffin-tin" radii of $R_{MT} = 2.75$ a.u. for Dy, $R_{MT} = 2.3$ a.u. for Cu, $R_{MT} = 1.25$ a.u. for C were used. The LAPW basis cutoff is defined by the condition $R^{Dy}_{MT} \times K_{\rm max} = 8.25$ (where $K_{\rm max}$ is the cutoff for LAPW basis set). The Slater integrals $F_0 = 7.00$ eV, and $F_2 = 9.77$ eV, $F_4 = 6.53$ eV, and $F_6 = 4.83$ eV were chosen to parametrize the Coulomb interaction term in Eq. (1), and

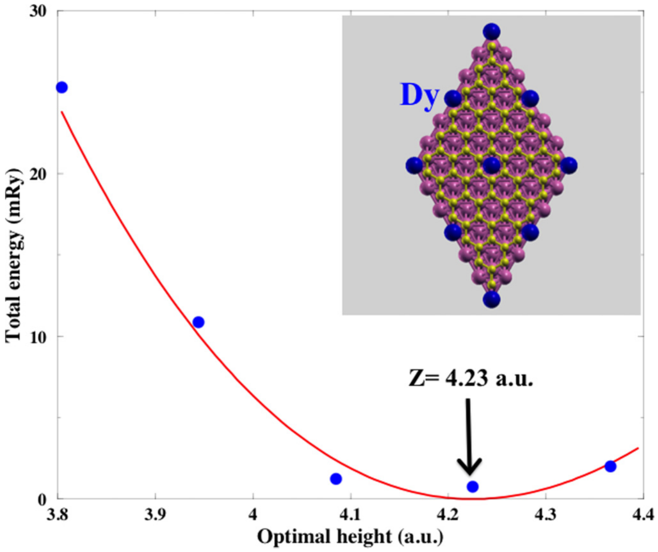

FIG. 1. Total energy vs distance between adatom and the surface (a.u.). Inset shows schematic supercell model for rare-earth impurity on graphene.

TABLE I. The f-electron occupation n_f, spin $\langle M_S\rangle$, orbital $\langle M_L\rangle$, $\langle M_S\rangle$ plus magnetic dipole $\langle M_D\rangle$ moments (in μ_B), and the ratio $R_{LS} = \frac{\langle M_L\rangle}{\langle M_S\rangle+\langle M_D\rangle}$ for the Dy adatom on GR/Cu(111) in comparison with available experimental XMCD [20]. Different AMF (Model A) and FLL (Model B) types of the double-counting are used.

Dy@GR/Cu	n_f	$\langle M_S\rangle$	$\langle M_L\rangle$	$\langle M_S\rangle + \langle M_D\rangle$	R_{LS}	XMCD R_{LS}
Model A	9.60	4.03	5.06	4.32	1.17	1.20 ± 0.2
Model B	9.88	3.74	5.97	4.69	1.27	

to construct the DFT + U potential V_U in Eq. (4). They corresponds to the values for Coulomb $U = 7.00$ eV and exchange $J = 0.82$ eV (see the Appendix for justification of the U and J parameters values).

The optimal height h_{Dy} for the rare-earth Dy adatom above the graphene surface layer was obtained from the total energy DFT + HIA calculations (see Fig. 1), and is equal to 4.225 a.u. In these calculations the Dy adatom was treated in a paramagnetic state. The calculated value of h_{Dy} is close to the optimal height of 4.235 a.u. that was obtained for the same placement of the Dy adatom on the top of GR/Ir(111) [19].

Next, we have performed the spin-polarized calculations assuming the z axis direction of the Dy adatom magnetization. In these calculations, we applied the non-spin-polarized exchange-correlation functional to the f states in Eq. (4) in order to exclude the contribution of f-intraorbital exchange field into the double-counting V_{dc}, while the spin-polarized functional is used for all other states. The exchange splitting $\Delta_{\text{EX}} = J_{fd} m_{5d}$ [16] is applied in Eq. (1), and evaluated self-consistently. Typically, the value of Δ_{EX} varies in the range between 5 and 20 meV during the calculations. Both AMF and FLL types of the double-counting V_{dc} were used. Further, we call the calculations with the AMF V_{dc} form as Model A, and with the FLL V_{dc} as Model B.

The calculated ground state f-electron occupation $n_f = \text{Tr}[\hat{n}]$, magnetic spin $\langle M_S\rangle = -2\langle S_z\rangle\mu_B/\hbar = -\text{Tr}[\hat{\sigma}_z\hat{n}]\mu_B/\hbar$, orbital $\langle M_L\rangle = -\langle L_z\rangle\mu_B/\hbar$, dipole $\langle M_D\rangle = -6\langle T_z\rangle\mu_B/\hbar$ moments, and $R_{LS} = \frac{\langle M_L\rangle}{\langle M_S\rangle+\langle M_D\rangle}$ value, the ratio of the orbital to the effective spin moment, are shown in Table I for both Models A and B, in comparison with the experimental XMCD data [20]. It is seen that there is only moderate difference in the ground state occupation, spin, and orbital magnetic moments between the two models. The total f occupation, which accounts for both the fully localized and itinerant contributions, is slightly increased in Model B. The spin moment $\langle M_S\rangle$ is slightly enhanced, while the orbital moment $\langle M_L\rangle$ is somewhat reduced when Model A is used. As a result, the use of AMF yields smaller R_{LS}-ratio than FLL, both in agreement with available XMCD data [20]. Thus, the DFT + U + HIA is not as sensitive to the choice of double-counting V_{dc}, as one would expect for conventional DFT + U applied to the f-electron systems [21].

In addition to the 4f-magnetic moment, Dy adatom 5d states create the $m_{5d} = 0.17\ \mu_B$ (Model A), 0.08 μ_B (Model B) magnetic moment. Note that the calculation of the m_{5d} moment is associated with some uncertainty, since this value will depend slightly on the choice of the Dy adatom muffin-tin radius. This value of m_{5d} yields the $\Delta_{\text{EX}} = 16$ meV (Model A), 7 meV (Model B) in Eq. (1).

The spin-resolved fDOS for Dy@GR/Cu is shown in Figs. 2(a) and 2(b). They are manifestly different for different choice of V_{dc}. In Model A, the occupied part of the spectrum, the spin-↑ manifold lies at around 6 to 12 eV below E_F, and spin-↓ states are at 5 to 6 eV. The unoccupied part sits right on the top of E_F. In Model B, both occupied and empty parts of the spectrum are shifted upwards by 3–4 eV. The graphene-layer-projected DOS are shown in Figs. 2(c) and 2(d). It is seen that the graphene zero band gap is located ≈ 1 eV below the Fermi level (E_F), indicating the n doping of graphene. They are very similar for both models.

The calculated total energy difference between two models A and B, $E_{\text{tot}}(\text{Model A}) - E_{\text{tot}}(\text{Model B}) = -0.5369$ Ry does not mean that the Model A solution is lower in the total energy than the Model B. Since the use of different double-counting V_{dc}, the total energies correspond to different total energy functionals, and can not be compared.

B. Calculation of XAS and XMCD spectra

We used the ionic Hamiltonian, Eq. (1), with the self-consistently determined parameters as an input for the Quanty code [22] to estimate the M-edge XAS and XMCD spectra. In these calculations, the exchange field Δ_{EX} is replaced with the external magnetic field $B_z = 6.8$ T typical in the experimental XMCD measurements [8]. The 3d−4f Coulomb interaction is parametrized with Slater integrals computed with the Cowan's Hartree-Fock code [23] and then reduced to 80% to approximately account for screening (Table II). The 3d spin-orbit coupling $\xi_{3d} = 14.4$ eV is taken from the same Hartree-Fock calculations.

Comparison of the computed spectra (Fig. 3) with available experimental data [24] points out Model B as more realistic. In particular, the very shallow XMCD spectrum found in Model A clearly disagrees with the experimental findings. The

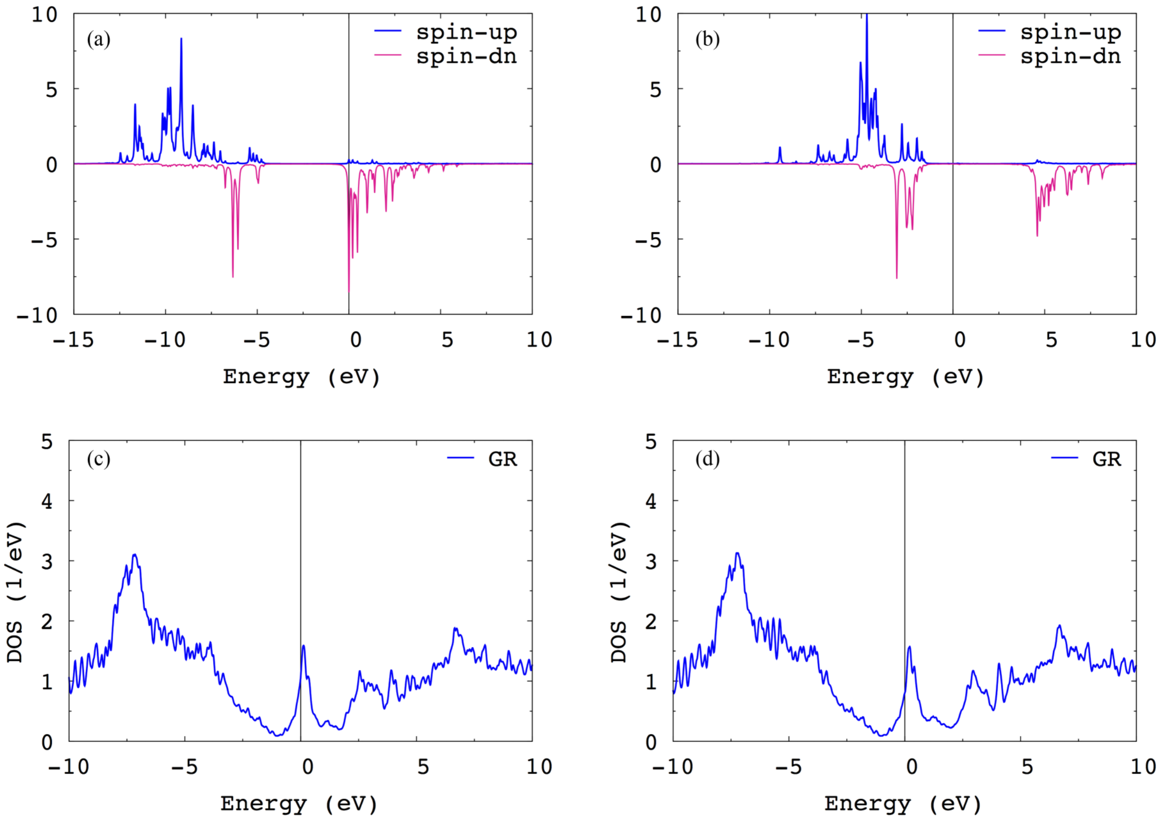

FIG. 2. The spin projected fDOS for the spin-polarized Dy@GR/Cu(111) (A Model A and (B) Model B; the graphene-layer-projected DOS for Dy@GR/Cu(111) (C) Model A and (D) Model B.

difference in XMCD spectra between models A and B can be traced to the difference in the ground state solutions of Eq. (1).

For Model A, the lowest energy state of Eq. (1) is a double-degenerate $|J = 7.5, J_z = \pm 0.48\rangle$ state. The f-shell quantum numbers are $N_f = 9$, $J = 7.5$, with Lande factor $g = 1.32$. They correspond to the f^9 ion configuration, and define the Dy adatom valence as Dy^{3+}. The scheme of quantum many-body levels of the lowest $J = 7.5$ multiplet is shown in Fig. 4(a). It is seen that the $|J = 7.5, J_z = \pm 0.48\rangle$ ground state corresponds to the "in-plane" magnetic moment orientation, and produces a weak and shallow XMCD signal shown in Fig. 3(a).

For Model B, the ground state of Eq. (1) is a doublet $|J = 8.0, J_z = \pm 8\rangle$. The f-shell quantum numbers are $N_f = 10$, $J = 8.0$, with Lande factor $g = 1.24$. They correspond to the f^{10} ion configuration, and define the Dy adatom valence as Dy^{2+}. Also, the $N_f = 10$ obtained from Eq. (1) is consistent with the f-electron occupation $n_f = 9.88$ (see Table I) calculated with the aid of Eq. (2). The corresponding scheme of quantum many-body levels of the lowest $J = 8$ multiplet is shown in Fig. 4(b). The $|J = 8, J_z = \pm 8\rangle$ ground state signals

TABLE II. Slater integrals defining the $3d$–$4f$ Coulomb interaction as computed with Cowan's code [23] for the XAS final states $3d^9 4f^{10}$ (Model A) and $3d^9 4f^{11}$ (Model B). The Hartree-Fock values are reduced to 80% to account for screening. All values are shown in eV.

	F_2	F_4	G_1	G_3	G_5
$3d^9 4f^{10}$	7.79	3.66	5.64	3.31	2.29
$3d^9 4f^{11}$	7.36	3.44	5.28	3.10	2.14

TABLE III. The nonzero CF parameters $[A_k^q \langle r^k \rangle]$ (meV) for Dy adatom on GR/Cu(111), and ZFS in comparison with Dy@GR/Ir(111) from Ref. [19]; the magnetic anisotropy constants K, and the corresponding magnetic anisotropy energy (MAE, meV).

Dy@GR/Cu	$A_2^0\langle r^2\rangle$	$A_4^0\langle r^4\rangle$	$A_6^0\langle r^6\rangle$	$A_6^6\langle r^6\rangle$	ZFS
Model A	−16.5	5.7	2.2	19.8	−20.4
Model B	−4.1	8.3	4.1	1.0	16.6
	K_1	K_2	K_3	K_4	MAE
Model A	−10.7	24.5	−29.6	1.2	−15.8
Model B	108.8	−207.1	110.4	−0.1	12.2
Dy@GR/Ir	$A_2^0\langle r^2\rangle$	$A_4^0\langle r^4\rangle$	$A_6^0\langle r^6\rangle$	$A_6^6\langle r^6\rangle$	ZFS
Model A [19]	−10.9	6.8	2.8	−7.5	8.1
Model B	−11.7	7.0	2.4	−5.8	6.2
	K_1	K_2	K_3	K_4	MAE
Model A	75.1	−144.6	75.1	0.9	5.6
Model B	67.8	−128.1	64.6	0.7	4.4

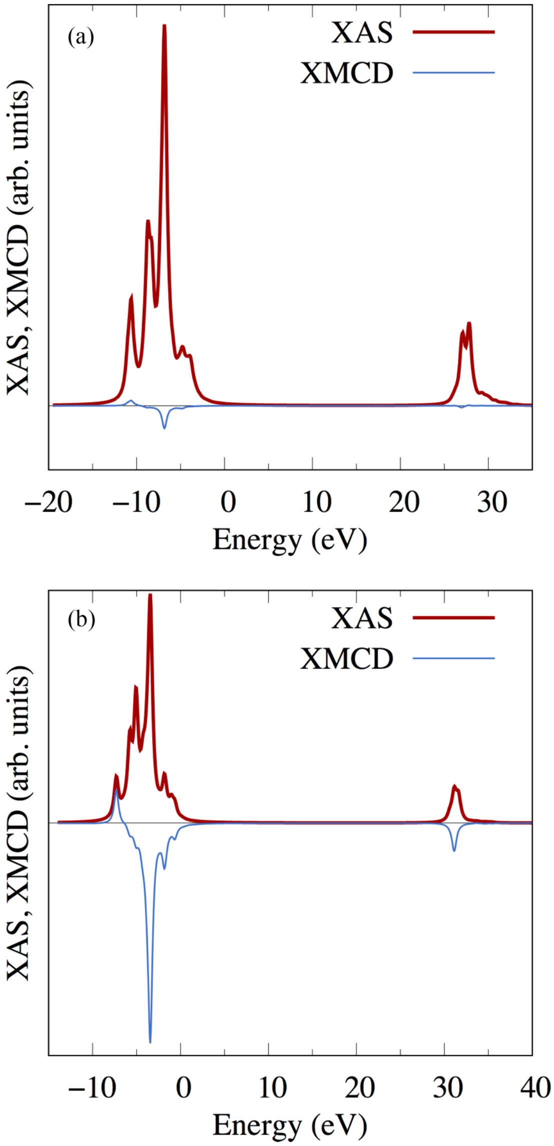

FIG. 3. XAS and XMCD (normal incidence) for Dy@GR/Cu(111): (A) for the case of Δ_{CF} and $\epsilon_f = -V_{dc}$ from Model A (AMF); (B) for the case of Δ_{CF} and $\epsilon_f = -V_{dc}$ from Model B (FLL).

the "out-of-plane" magnetic moment orientation, and yields a very different XMCD spectrum shown in Fig. 3(b).

C. Crystal-field model parameters

In previous work [19] we demonstrated that the CF Hamiltonian can be build from the results of the charge density self-consistent DFT + HIA calculations. The calculated $\Delta_{\rm CF}$ matrix is used to build the CF Hamiltonian for the Dy@GR/Cu(111),

$$\hat{H}_{CF} = \sum_{kq} A_k^q \langle r^k \rangle \Theta_k(J) \hat{O}_k^q \ , \quad (5)$$

where $\hat{O}_k^q$ are the Stevens operator equivalents, $\Theta_k(J)$ are the Stevens factors for a given ground state multiplet J, and $A_k^q\langle r^k\rangle$, the CF parameters (in standard notations) for given k and q. Note that $\Theta_k(J)$ for $k = 2, 4$, and 6 are often designated by α_J, β_J, and γ_J, respectively.

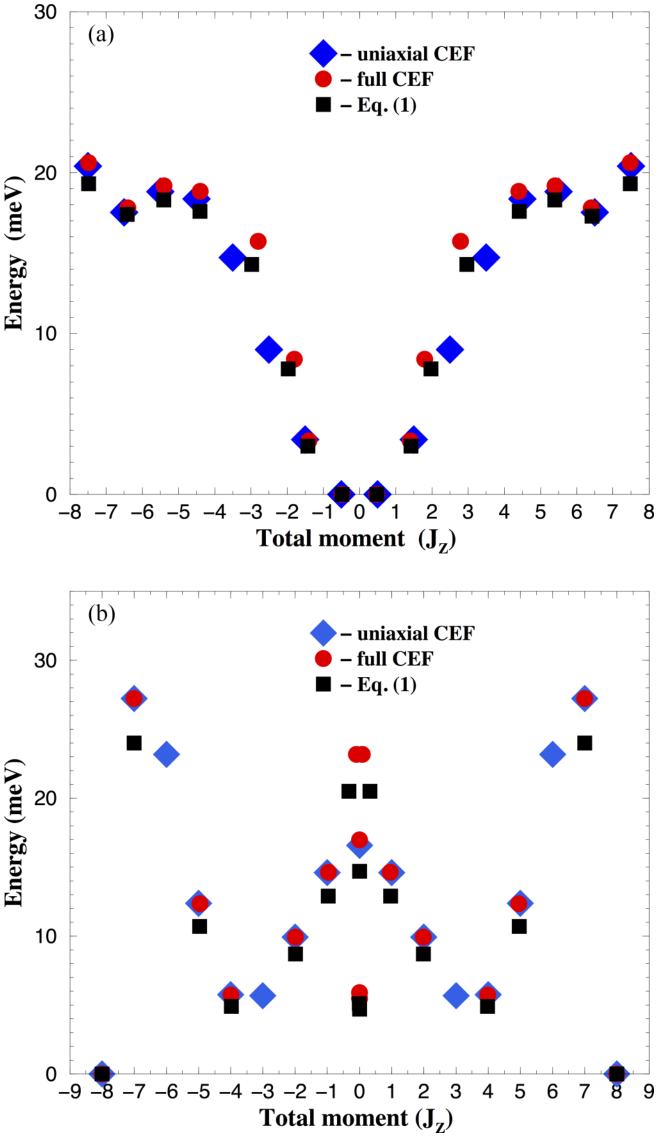

FIG. 4. Scheme of quantum many-body levels of the lowest $J = 7.5$ multiplet obtained from the nonmagnetic solutions ($\Delta_{\rm ex} = 0$) of Eq. (1) with the $\Delta_{\rm CF}$ parameters taken from spin-polarized calculations (squares); energy diagram of the CF Hamiltonian with the CF parameters from Table III (circles), and the uniaxial CEF only (diamonds).

The calculated nonzero CF parameters $A_k^q\langle r^k\rangle$ for Dy adatom on Cu(111) are shown in Table III for both models A and B. The corresponding energy diagram of the CF Hamiltonian Eq. (5) with the CF parameters given in Table III are show in Fig. 4(a) for Model A, and in Fig. 4(b) for Model B. It is seen that the CF solutions approximate very well the many-body solutions of the Eq. (1) for both models A and B.

The first three CF parameters yield the uniaxial splitting of different J_z eigenstates in Eq. (5). They determine the energy difference between the lowest and highest J_z levels, the so-called ZFS. The ZFS is shown in Table III. It is negative for Model A, and positive for Model B. Obviously, negative ZFS corresponds to the "in-plane", and positive ZFS to the "out-of-plane" orientation of the magnetic moment. Thus, ZFS is related to the uniaxial MAE defined as the total energy gain due to the magnetization rotation from "out-of-plane" to the "in-plane" direction, and negative value of MAE means the "in-plane" orientation of the magnetic moment.

Following the recipe of the CF theory [25], the magnetic anisotropy $E_{MA}(\theta,\phi)$ can be identified as a diagonal element $\langle J, J_z = J|\,\hat{H}_{CF}\,|J, J_z = J\rangle$, where the polar (θ,ϕ) angles specify the magnetization direction. For Dy adatom on Cu(111), the magnetic anisotropy is then written as

$$E_{MA} = K_1 \sin^2\theta + K_2 \sin^4\theta + K_3 \sin^6\theta + K_4 \sin^6\theta \cos(6\phi). \tag{6}$$

The magnetic anisotropy constants $K_{1,2,3,4}$ in Eq. (6) can be expressed as linear combinations of the coefficients $B_k^q = A_k^q\langle r^k\rangle\Theta_k(J)$ [25].

The magnetic anisotropy constants calculated for Dy@GR/Cu(111) are shown in Table III. The first three parameters $K_{1,2,3}$ describe the uniaxial anisotropy, and K_4 is responsible for the "in-plane" anisotropy. Then the uniaxial MAE can be expressed in terms of E_{MA} Eq. (6), MAE $= E_{MA}(\theta = \pi/2) - E_{MA}(\theta = 0)$. For both models A and B, the uniaxial MAE is in good semiquantitative agreement with ZFS.

The choice of the appropriate double-counting model is made by comparison with XMCD experiments. This comparison suggests the Model B (FLL V_{dc}), with divalent Dy^{2+} adatom, and positive magnetic anisotropy being consistent with currently available experimental data [20,24], and we will use this model in the following discussion.

Now we compare the calculated properties of Dy@GR/Cu(111) and Dy@GR/Ir(111) described in Ref. [19]. Both models A and B give similar results for Dy@GR/Ir(111) (see Table III), and we focus on the comparison between the results of the model B calculations. For Dy@GR/Ir(111) both the spin $M_S = 3.57\ \mu_B$ and the orbital $M_L = 5.71\ \mu_B$ are slightly reduced in a comparison with Dy@GR/Cu(111) (see Table I). This similarity is not surprising taking into account similarity in optimal height h_{Dy} in the two systems. The CF parameters are changing more substantially, and corresponding ZFS differs by almost a factor of 3. The MAE of Dy@GR/Ir(111) is positive but smaller than the MAE of Dy@GR/Cu(111).

IV. DISCUSSION

The magnetic stability of SAM requires the ground state doublet $|J = 8.0, J_z = \pm 8\rangle$ not to be mixed in the CF symmetry. The transverse CF parameter $A_6^6\langle r^6\rangle$ in Table III couples different J_z states, since the matrix element $\langle J_z = m|\,\hat{O}_6^6\,|J_z = n\rangle \neq 0$ for $|m-n| = 6, 12$. The ground-state doublet $J_z = \pm 8$ remains unchanged by this transversal term [see Fig. 4(b)]. The quantum tunneling of the magnetization (QTM) occurs for $|J = 8.0, J_z = \pm 6\rangle$ and $|J = 8.0, J_z = \pm 3\rangle$ states. The energy barrier for the magnetization reversal defined by the uniaxial MAE of 12 meV (Table III) is then substantially reduced to 5 meV.

The magnetic moment reversal can be triggered by scattering with itinerant electrons. The coupling between $4f$ magnetization, and the substrate itinerant electrons is mediated by the exchange interaction, which we consider for simplicity in the form $J_K(g_J - 1)\sum_{k,\sigma,\sigma'}(\vec{J}\,\vec{\sigma}_{\sigma,\sigma'}/2)c^{\dagger}_{k\sigma}c_{k\sigma'}$ [26], where J_K is the so-called Kondo exchange, g_J is the Lande factor, the $c^{\dagger}$, c are creation and annihilation operators for the itinerant $|k,\sigma\rangle$ state. The coupling strength [27] can be obtained from the hybridization function $\Delta(E_F) = \frac{1}{\pi}\,\mathrm{Im\,Tr}[G^{-1}_{\mathrm{HIA}}(E_F + i0)])$ [28],

$$J_K N(E_F) = 2\frac{\Delta(E_F)}{N_f}\left[\frac{1}{(\epsilon_{\mathrm{f}} + U - J)} - \frac{1}{\epsilon_{\mathrm{f}}}\right] \tag{7}$$

where $N(E_F)$ is the DOS of the itinerant electrons coupled to the localized $4f$ moment, $N_f = 14$ is the f-states degeneracy, and ϵ_f is a location of the $4f$ energy level. We obtain $\Delta(E_F) = 0.16$ eV, and $J_K N(E_F) = 0.23$ for Dy@GR/Cu(111). This value of coupling strength is smaller than $J_K N(E_F) = 0.57$ estimated for Dy@GR/Ir(111) [19]. We interpret it as a reduction of the exchange coupling between the f shell and conduction electrons in Dy@GR/Cu(111).

We can make an estimate for the spin-flip energy E_{sf}, making use of the $N(E_F) = 0.34$ 1/eV and $m = 0.08\ \mu_B$ for the non-fDOS and the magnetic moment of the Dy-atom muffin-tin sphere, and obtain $E_{sf} \approx 104$ meV. This energy exceeds substantially the 16.6 meV ZFS energy barrier (Table III). Further, considering the selection rules for the spin-flip transitions $J_z \to J_z, J_z \pm 1$, we find [see Fig. 4(b)] that the system can transit from $|J = 8, J_z = 8\rangle$ to $|J = 8, J_z = 7\rangle$, which is 27 meV higher. The next allowed transition would be to the $|J = 8, J_z = 6\rangle$, but the transverse CF parameter $A_6^6\langle r^6\rangle$ couples $|J = 8.0, J_z = \pm 6\rangle$ states, transforming them into the doublet with $J_z \approx 0$ at the energy of 23 meV. Thus the scattering due to itinerant electrons can, at least in principle, activate the QTM induced magnetic reversal. Moreover, the CF symmetry distortions owing to the nonequivalence of the two carbon sublattices in graphene can provide additional paths for the magnetic relaxation.

Another source of the magnetic reversal is the interaction of the magnetic moment with the surface vibrations. Due to a weak coupling of graphene to the Cu substrate [29], it is reasonable to assume that graphene phonon modes play a role in the Dy adatom magnetic reversal. From six phonon branches of pristine graphene [30], the acoustic out-of-plane ZA mode is shifted by $\omega_0 \sim 6$ meV near the Γ point [31] due to interaction with Cu(111) substrate. This energy is comparable with the 5 meV energy barrier due to quantum tunneling between $|J = 8.0, J_z = \pm 3\rangle$ states. Thus perpendicular vibrations of graphene in a combination with QTM can contribute to the magnetic reversal.

Finally, we consider an effect of the Dy adatom vibrations on the magnetic reversal. From the total energy dependence on the distance h_{Dy} between the adatom and the surface, shown in Fig. 1 for Dy@GR/Cu(111) and in Fig. 1(b) of Ref. [19] for Dy@GR/Ir(111), the second derivative d^2E/d^2h can be calculated. Then the quantum of vibrational energy $\hbar\omega$ of 30.05 meV for Dy@GR/Cu(111), and 38.3 meV for Dy@GR/Ir(111) is estimated.

For Dy@GR/Cu(111), the energy difference $\Delta_{\Uparrow\to\Downarrow}$ between the ground state $|J = 8.0, J_z = 8\rangle$ and the excited state $|J = 8.0, J_z = 7\rangle$ is equal to 27.2 meV [see Fig. 4(b)].

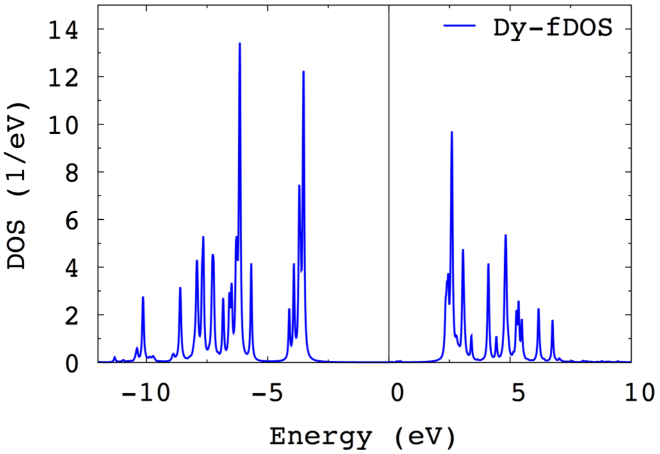

FIG. 5. f-orbital DOS for the bulk hcp-Dy calculated with DFT + HIA.

Thus, $\Delta_{\Uparrow\to\Downarrow} \approx \hbar\omega$, and the transition between these two states can be triggered by a quantum of vibration. Without QTM, the $|J = 8.0, J_z = 7\rangle$ can transit to the lower energy $|J = 8.0, J_z = 6\rangle$ state. However, quantum tunneling between $|J = 8.0, J_z = \pm 6\rangle$ states transforms them to the doublet $|J = 8.0, J_z = 0\rangle$ at the energy of 23 meV [see Fig. 4(b)]. Thus, the z-axis projection of the magnetization goes to zero, and Dy@GR/Cu(111) becomes demagnetized.

No such scenario is possible for Dy@GR/Ir(111) since $\hbar\omega = 38.3$ meV is substantially larger that $\Delta_{\Uparrow\to\Downarrow} = 17.0$ meV [19]. Thus, the ground state $|J = 8.0, J_z = 8\rangle$ remains protected against the Dy atom vibration. Experimentally, the magnetic remanence was found for Dy@GR/Ir(111) [6,24], and no clear remanence was observed for Dy adatoms deposited on graphene grown on polycrystalline Cu foil [24]. The crossover $\Delta_{\Uparrow\to\Downarrow} \approx \hbar\omega$, which is found in Dy@GR/Cu(111), can explain this different magnetic behavior.

V. SUMMARY

The electronic structure and magnetism of individual Dy atoms adsorbed on the graphene/Cu(111) surface is investigated using the combination of the density functional theory with the Hubbard-I approximation to the Anderson impurity model (DFT + U + HIA). We find that the electronic structure, spin and orbital magnetic moments and the MAE of the Dy adatom depend on the choice of the double-counting term in DFT + U + HIA. For FLL V_{dc}, the divalent Dy^{2+} adatom is found, with the magnetic moment of 9.71 μ_B. The spin and orbital magnetic moments are evaluated and compared with the XMCD data. The positive magnetic anisotropy energy determines the out-of-plane orientation of the Dy adatom magnetic moment, in qualitative agreement with available experimental data.

ACKNOWLEDGMENTS

We acknowledge stimulating discussions with S. Rusponi and A. Barla. Financial support was provided by Operational Programme Research, Development and Education financed by European Structural and Investment Funds and the Czech Ministry of Education, Youth, and Sports (Project No. SOLID21 - CZ.02.1.01/0.0/0.0/16_019/0000760), Mobility Plus Project No. CNR-19-03 of the Czech Academy of Sciences, and by the Czech Science Foundation (GACR) Grant No. 18-06240S. D. S. Shapiro acknowledges the funding by Russian Foundation for Basic Research according to the Project No. 20-37-70028.

APPENDIX: CHOICE OF COULOMB U AND EXCHANGE J

In order to justify our choice of the Coulomb U and exchange J parameters, we have performed the DFT + HIA calculations for the bulk Dy in the paramagnetic state for the experimental lattice parameters (a and c/a ratio). The resulting fDOS is shown in Fig. 5. The DFT + HIA results are in agreement with the experimental data [32] for both the occupied and empty $4f$ states. Comparison with experimental valence-band photoelectron spectroscopy is often taken as important criterion of truthfulness of electronic structure calculations.

We assume the transferability of the Coulomb $U = 7$ eV and exchange $J = 0.82$ eV values, and use them in the Dy@GR/Cu(111) calculations. Note that these values of U and J are in the ballpark of commonly accepted values for rare earths [33].

[1] F. Donati, A. Singha, S. Stepanow, C. Wäckerlin, J. Dreiser, P. Gambardella, S. Rusponi, and H. Brune, Phys. Rev. Lett. **113**, 237201 (2014).

[2] M. Steinbrecher, A. Sonntag, M. dos Santos Dias, M. Bouhassoune, S. Lounis, J. Wiebe, R. Wiesendanger, and A. A. Khajetoorians, Nat. Commun. **7**, 10454 (2016).

[3] F. Donati, S. Rusponi, S. Stepanow, C. Wäckerlin, A. Singha, L. Persichetti, R. Baltic, K. Diller, F. Patthey, E. Fernandes, J. Dreiser, Ž. Šljivančanin, K. Kummer, C. Nistor, P. Gambardella, and H. Brune, Science **352**, 318 (2016).

[4] P. R. Forrester, F. Patthey, E. Fernandes, D. P. Sblendorio, H. Brune, and F. D. Natterer, Phys. Rev. B **100**, 180405(R) (2019).

[5] L. K. Grover, Phys. Rev. Lett. **79**, 325 (1997).

[6] R. Baltic, M. Pivetta, F. Donati, C. Wäckerlin, A. Singha, J. Dreiser, S. Rusponi, and H. Brune, Nano Lett. **16**, 7610 (2016).

[7] B. T. Thole, P. Carra, F. Sette, and G. van der Laan, Phys. Rev. Lett. **68**, 1943 (1992).

[8] A. Singha, R. Baltic, F. Donati, C. Wäckerlin, J. Dreiser, L. Persichetti, S. Stepanow, P. Gambardella, S. Rusponi, and H. Brune, Phys. Rev. B **96**, 224418 (2017).

[9] V. I. Anisimov, J. Zaanen, and O. K. Andersen, Phys. Rev. B **44**, 943 (1991).

[10] I. V. Solovyev, P. H. Dederichs, and V. I. Anisimov, Phys. Rev. B **50**, 16861 (1994).

[11] A. B. Shick, A. I. Liechtenstein, and W. E. Pickett, Phys. Rev. B **60**, 10763 (1999).

[12] A. B. Shick and W. E. Pickett, Phys. Rev. Lett. **86**, 300 (2001).
[13] A. Hewson, *The Kondo Problem to Heavy Fermions*, (Cambridge University Press, Cambridge, 1993).
[14] J. Kolorenč, A. I. Poteryaev, A. I. Lichtenstein, Phys. Rev. B **85**, 235136 (2012).
[15] O. Kristanovski, A. B. Shick, F. Lechermann, and A. I. Lichtenstein, Phys. Rev. B **97**, 201116(R) (2018).
[16] L. Peters, I. Di Marco, P. Thunström, M. I. Katsnelson, A. Kirilyuk, and O. Eriksson, Phys. Rev. B **89**, 205109 (2014).
[17] M. Brooks, O. Eriksson, and B. Johansson, J. Phys.: Condens. Matter **1**, 5861 (1989).
[18] P. A. Khomyakov, G. Giovannetti, P. C. Rusu, G. Brocks, J. van den Brink, and P. J. Kelly, Phys. Rev. B **79**, 195425 (2009).
[19] A. B. Shick, A. Yu. Denisov, J. Magn. Magn. Mater. **475**, 211 (2018).
[20] S. Rusponi (private communication, 2018). Note that the measurements were done for Dy deposited on graphene grown on polycrystalline Cu.
[21] A. B. Shick, V. Drchal, and L. Havela, Europhys. Lett. **69**, 588 (2005).
[22] M. W. Haverkort, M. Zwierzycki, and O. K. Andersen, Phys. Rev. B **85**, 165113 (2012).
[23] R. D. Cowan, *The Theory of Atomic Structure and Spectra* (University of California Press, Berkeley, CA, 1981).
[24] R. Baltic, Ph.D. thesis, Ecole Polytechnique Fédérale de Lausanne, Switzerland (2018).
[25] J. F. Herbst, Rev. Mod. Phys. **63**, 819 (1991).
[26] Ch. Karlewski, M. Marthaler, T. Märkl, T. Balashov, W. Wulfhekel, and G. Schön, Phys. Rev. B **91**, 245430 (2015).
[27] J. Schrieffer and P. Wolf, Phys. Rev. **149**, 491 (1966).
[28] J. E. Han, M. Alouani, and D. L. Cox, Phys. Rev. Lett. **78**, 939 (1997).
[29] A. Al-Taleb, H. K. Yu, G. Anemone, D. Farias, and A. M. Wodtke, Carbon **95**, 731 (2015).
[30] M. Katsnelson, *Graphene* (Cambridge University Press, Cambridge, 2012).
[31] L. Chen, Z. Huang, and S. Kumar, Appl. Phys. Lett. **103**, 123110 (2013).
[32] S. Lang, Y. Baer, and P. Cox, J. Phys. F **11**, 121 (1981).
[33] D. van der Marel and G. A. Sawatzky, Phys. Rev. B **37**, 10674 (1988).